

Final Report on  
ONR Grant No. N00014-99-1-0471

**SCIENCE UNDERPINNING TBC DESIGN FOR  
DURABILITY IN AGGRESSIVE ENVIRONMENTS**

*Principal Investigator:*

**Carlos G. Levi**

Materials Department, University of California  
Santa Barbara, CA 93106-5050  
levic@engineering.ucsb.edu

*Submitted to:*



**Office of Naval Research**

Attention: Dr. David A. Shifler  
875 N. Randolph Street, Suite 1425  
ONR 332, Room 631  
Arlington, VA 22203-1995

October 1, 2008

**20081020200**

**REPORT DOCUMENTATION PAGE**

*Form Approved  
OMB No. 0704-0188*

The public reporting burden for this collection of information is estimated to average 1 hour per response, including the time for reviewing instructions, searching existing data sources, gathering and maintaining the data needed, and completing and reviewing the collection of information. Send comments regarding this burden estimate or any other aspect of this collection of information, including suggestions for reducing the burden, to the Department of Defense, Executive Service Directorate (0704-0188). Respondents should be aware that notwithstanding any other provision of law, no person shall be subject to any penalty for failing to comply with a collection of information if it does not display a currently valid OMB control number.

**PLEASE DO NOT RETURN YOUR FORM TO THE ABOVE ORGANIZATION.**

<b>1. REPORT DATE (DD-MM-YYYY)</b> 16-10-2008	<b>2. REPORT TYPE</b> Final Technical Report	<b>3. DATES COVERED (From - To)</b> 4/1/99 - 6/30/08
--	---	---

<b>4. TITLE AND SUBTITLE</b> Science Underpinning TBC Design for Durability in Aggressive Environments	<b>5a. CONTRACT NUMBER</b>
	<b>5b. GRANT NUMBER</b> N00014-99-1-0471
	<b>5c. PROGRAM ELEMENT NUMBER</b>

<b>6. AUTHOR(S)</b> Carlos G. Levi	<b>5d. PROJECT NUMBER</b>
	<b>5e. TASK NUMBER</b>
	<b>5f. WORK UNIT NUMBER</b> 332

<b>7. PERFORMING ORGANIZATION NAME(S) AND ADDRESS(ES)</b> The Regents of the University of California, Santa Barbara Office of Research Cheadle Hall, Room 3227 Santa Barbara, CA 93106-2050	<b>8. PERFORMING ORGANIZATION REPORT NUMBER</b>
--	---

<b>9. SPONSORING/MONITORING AGENCY NAME(S) AND ADDRESS(ES)</b> Office of Naval Research 140 Sylvester Road Bldg., 140, Room 218 San Diego, CA 92106-3521	<b>10. SPONSOR/MONITOR'S ACRONYM(S)</b> ONR
	<b>11. SPONSOR/MONITOR'S REPORT NUMBER(S)</b>

**12. DISTRIBUTION/AVAILABILITY STATEMENT**  
"Approved for Public Release; Distribution is Unlimited."

**13. SUPPLEMENTARY NOTES**

**14. ABSTRACT**  
The aims of this research were the scientific understanding of the environmental degradation of thermal barrier systems by molten deposits, as relevant to the US Navy aircraft and marine engines, and the application of this understanding to develop mitigation strategies. The program had two thrusts, one addressing molten deposits of calcium-magnesium aluminosilicates (CMAS), and the other the corrosive sulfate/vanadate (S/V) melts resulting from salt ingestion combined with fuel contaminants. In principle, both types of deposits can penetrate the coating and reduce its compliance upon freezing, leading to thermomechanical damage, but also attack thermochemically the TBC by dissolving the barrier oxide and reprecipitating undesirable phases. The program successfully elucidated the mechanisms and identified mitigating strategies for both problems. The proposed CMAS mitigation is based on reaction with a rare earth zirconate layer, which leads to the precipitation of solid phases in sufficient volume to inhibit the capillary-driven flow of CMAS into the pore spaces of the coating. The approach for S/V relied on reducing the Y activity by co-doping with Ta. The latter compositions also offer phase stability at considerably higher temperatures than 7YSZ and attractive toughness.

**15. SUBJECT TERMS**

<b>16. SECURITY CLASSIFICATION OF:</b>			<b>17. LIMITATION OF ABSTRACT</b>	<b>18. NUMBER OF PAGES</b>	<b>19a. NAME OF RESPONSIBLE PERSON</b> Carlos G. Levi
<b>a. REPORT</b>	<b>b. ABSTRACT</b>	<b>c. THIS PAGE</b>			<b>19b. TELEPHONE NUMBER (Include area code)</b> 805.893.2381

## Synopsis

This program was part of a longer-term effort to provide scientific insight into the environmental degradation of thermal barrier systems by molten deposits, as relevant to the US Navy aircraft and marine engines, and to apply the emerging understanding to develop mitigation strategies. During the funding period covered by this report the program had two major thrusts, one addressing the higher temperature deposits of calcium-magnesium aluminosilicates (CMAS) resulting from the ingestion of siliceous debris into the engines, and the other the corrosive sulfate/vanadate melts resulting from the combination of salt ingestion in marine environments with contaminants in the fuel. In principle, both types of deposits can penetrate the coating and reduce its compliance upon freezing, leading to thermomechanical damage, but also attack thermochemically the TBC by dissolving the barrier oxide and re-precipitating phases that are often (albeit not always) less desirable.

The initial goals of the thrust on S/V melt attack were accomplished, including both the elucidation of the corrosion mechanism and the identification of a mitigation approach involving Y+Ta co-doping of zirconia. It was shown that the co-doped compositions are superior in corrosion to those involving Y doping alone, even under very aggressive conditions of high  $p\text{SO}_3$ . Selected compositions in this system also proved to be phase stable to temperatures up to 1500°C, concurrent with comparable or higher toughness than conventional YSZ compositions, wherein long-term phase stability becomes a problem above ~1300°C.

The CMAS thrust focused on understanding the mechanisms and kinetics of the dissolution and re-precipitation processes and their effects on infiltration dynamics, with emphasis on vapor-grown segmented columnar coatings. Of particular interest is the discovery that CMAS penetration is inhibited in zirconate TBCs that are of interest as lower conductivity thermal barrier oxides, including those of Gd and Y as prototypes for the pyrochlore and delta-phase structures, respectively. The fundamental concept underlying this mitigating strategy is the conversion of the CMAS melt into crystalline phases by reaction with the solid zirconate. The primary crystalline products include an apatite silicate based on the composition  $\text{Ca}_2(\text{Gd}/\text{Y},\text{Zr})_8(\text{SiO}_4)_6\text{O}_2$ , and a fluorite solid solution  $(\text{Zr},\text{Gd}/\text{Y},\text{Ca})\text{O}_2$ , with minor phases including spinel and a secondary crystalline silicate. It has been shown that the reaction is competitive with the dynamics of melt penetration into the intercolumnar gaps of the structure, leading to the rapid sealing of the flow paths into the coating. Subsequent attack of the coating proceeds much more slowly reducing the potential for spallation and subsequent re-exposure of the TBC to CMAS.

The mitigating approaches for both S/V and CMAS melts have been transferred to industry and their implementation is being explored by one major engine manufacturer, and in the case of the CMAS-resistant zirconates has already been demonstrated in field tests by another major OEM.

### **CMAS Thrust**

CMAS penetration into the TBC leads to a loss of compliance and the eventual spallation of the coating under thermal cycling [1, 2] (Fig. 1). Modeling under separate ONR funding has identified various scenarios under which spallation of the stiffened layer may occur [2-4]. A key parameter is the depth of penetration, which dictates the stiffened layer thickness and in the few field specimens available was found to be of the order of half the total TBC thickness. Much of the emphasis has thus been on understanding the infiltration kinetics and the phenomena that lead to the arrest of the penetration into the coating. Experiments in this period included primarily isothermal exposures to a model CMAS of composition  $\text{Ca}_{33}\text{Mg}_9\text{Al}_{13}\text{Si}_{45}$ , corresponding to typical silicate melts found within the pore spaces of engine components after service [1].

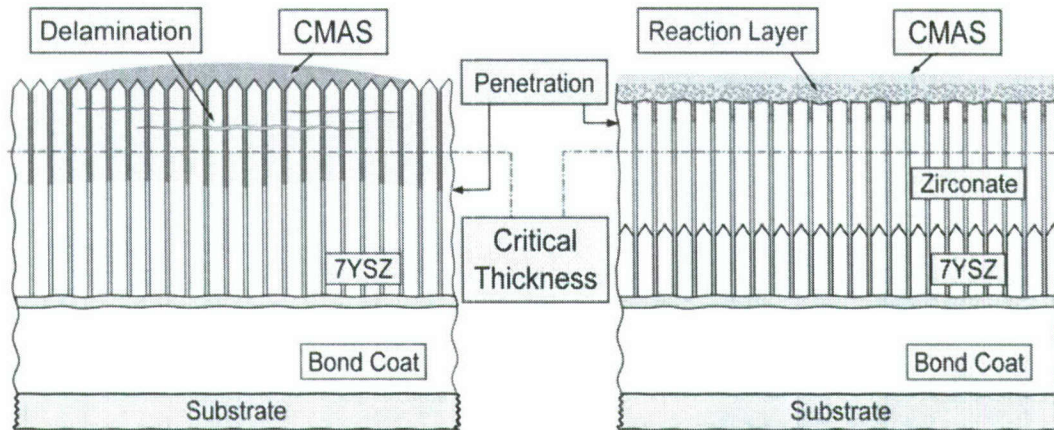


Fig. 1. TBC failure by delamination due to CMAS impregnation (left), and mitigation concept using an alternate oxide that reacts with the CMAS melt and converts it into crystalline phases near the surface (right). The critical thickness to induce delamination is assumed constant for illustration purposes only, but can be estimated with existing thermomechanical models

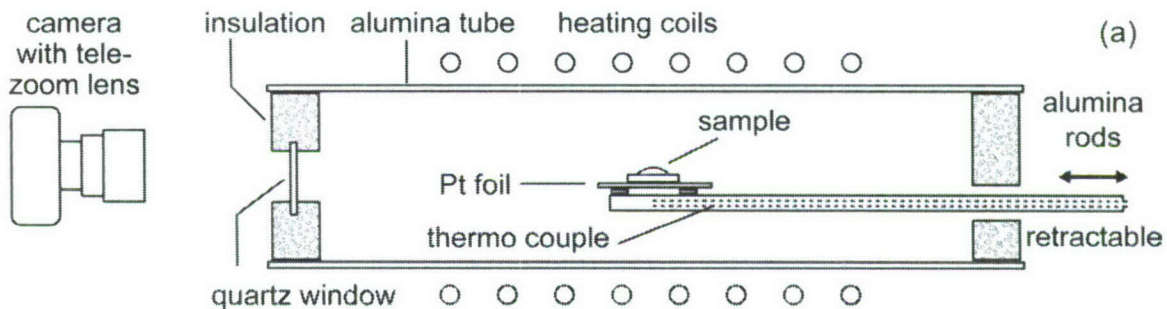


Fig. 2. The experimental set up used for the visualization experiments. The sample is initially equilibrated at a prescribed temperature below the melting point of the model CMAS, ~1200°C. After equilibration the sample is rapidly moved into the hot zone, which is at a higher prescribed temperature, typically 1250-1300°C, held for a prescribed time and then removed to cooled rapidly in the cold zone.

The experimental set up is schematically illustrated in Fig. 2. Coupons 25 x 25mm were generated in-house by EB-PVD of 7YSZ, or  $Gd_2Zr_2O_7/Y_4Zr_3O_{12} + 7YSZ$  bilayers on polycrystalline alumina substrates. Deposition was performed at 1000°C, ~2µm/min and a rotation rate of 8rpm. The coupons were sectioned into smaller pieces and a small pellet of CMAS was placed on each. (The pellet was fabricated by mixing the elemental oxides, calcining, pressing the mixture into a small disk and sintering at 1200°C). The coating+CMAS assemblage was then placed on a Pt-foil covered alumina plate attached at the end of two parallel rods and a thermo-couple was placed close to the sample. The rod, mounted on a suitable displacement mechanism, was then inserted into a preheated tube furnace to a location in which the temperature is ~1200°C, below the melting point of the model CMAS (~1240°C). Once the sample is equilibrated the assemblage is moved rapidly into the hot zone, pre-set at a temperature ranging from 1250°C to 1300°C, and held for a prescribed time while its temperature is monitored. After the desired time has elapsed the sample is moved back to the cold end of the furnace and allowed to cool. The sample was then sectioned, polished, photographed optically to document the shape of the pellet and any evident interaction, and then subjected to closer examination by SEM and TEM. In some experiments the melting and spreading behavior were documented using a camera equipped with a telescopic zoom.

### Findings

Literature data on viscosity and glass transition temperatures (typically 700-800°C) for silicate glasses of CMAS-like composition suggest that the melt is sufficiently fluid at the temperatures prevailing within the TBC that its penetration can only be arrested effectively by inducing crystallization. Indeed, all field specimens examined had crystallized CMAS at the bottom of the penetrated zone [4], and in some cases throughout the thickness. Analysis suggested that the melt crystallizes when it reaches an undercooling of ~100-150°C [4], whereas absent a thermal gradient the CMAS penetrates throughout a ~200µm 7YSZ coating in times of the order of ~1 min or less [5]. The inference is that the key to limit penetration is to make the crystallization kinetics competitive with the capillarity-driven flow of the melt into the coating so that the melt is induced to crystallize as close as possible to the surface (Fig. 1). The approach involves modifying the melt chemistry by rapid dissolution of the thermal barrier or an alternate sacrificial oxide at the surface. Given that the time scale of the penetration process is ≤1 min, the kinetics of dissolution and crystallization must be sufficiently fast to consume the melt as it penetrates and convert it into solid phases.

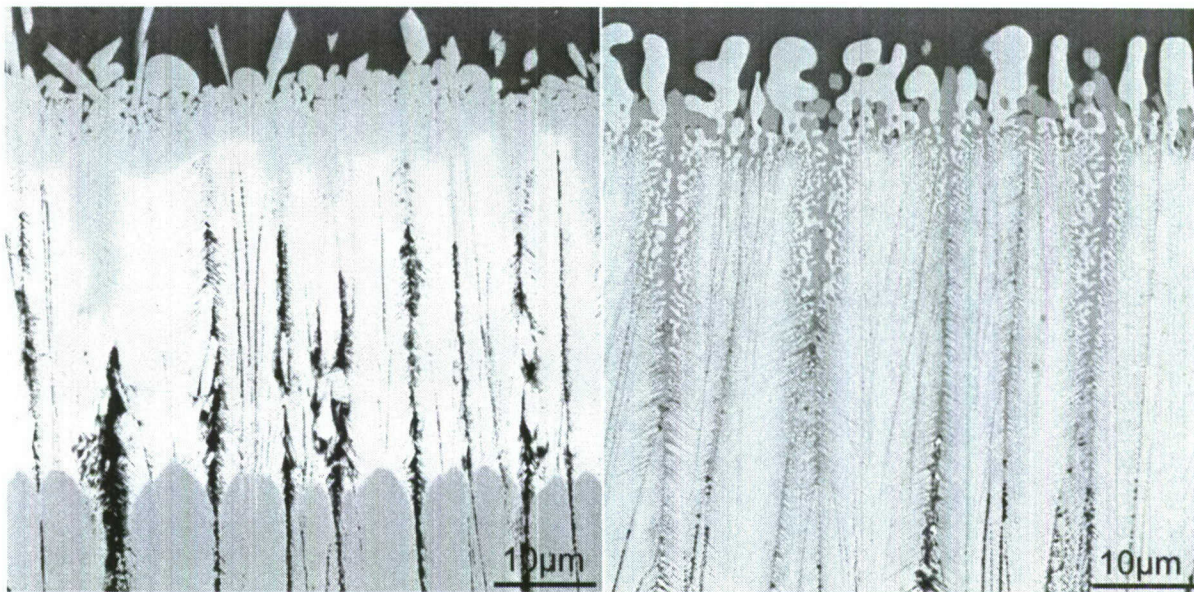


Fig. 3. Comparison of the interaction zones when CMAS reacts with  $Gd_2Zr_2O_7$  (left) and  $Y_4Zr_3O_{12}$  (right). Both zirconates are deposited by electron beam evaporation on alumina substrates with a 7YSZ interlayer to avoid the thermochemical interaction between the zirconate and the substrate [6]. The coatings were exposed to a model CMAS of composition  $Ca_{33}Mg_9Al_{13}Si_{45}$  for 4 h at 1300°C. The penetration along the intercolumnar gaps is somewhat deeper in the Y zirconate, but in both cases it is limited to ≤40µm, or about 20% of the thickness of the coating. Conversely, the reaction with the column tips appears to be somewhat greater for the Gd zirconate.

When the TBC is based on  $Gd_2Zr_2O_7$  (prototypical of zirconates with the pyrochlore structure) or  $Y_4Zr_3O_{12}$  (prototypical of the delta-phase zirconates) CMAS penetration stops at about 20-40µm below the surface *even under isothermal conditions* (Fig. 3). (In principle, the stiffened layer should be even thinner under a thermal gradient.) The observations suggest that zirconate based TBCs, which were originally identified as attractive substitutes for 7YSZ in TBCs because of their substantially lower thermal conductivity [7-11] and sintering resistance [12], offer additional benefits when CMAS attack is a concern [13]. Issues with zirconates as TBCs are their relatively lower toughness [14] and tendency to react with the TGO [6], but these could be alle-

viated using zirconates in combination with a 7YSZ underlayer (cf. Fig. 3). Interactions with Pratt & Whitney have revealed that the results of this program are consistent with recently disclosed field observations on Gd-zirconate (GZ) based low-k TBCs [15]. The program has also collaborated closely with GE Aviation in implementing and testing bi-layer concepts based on combinations of zirconates and YSZ [16].

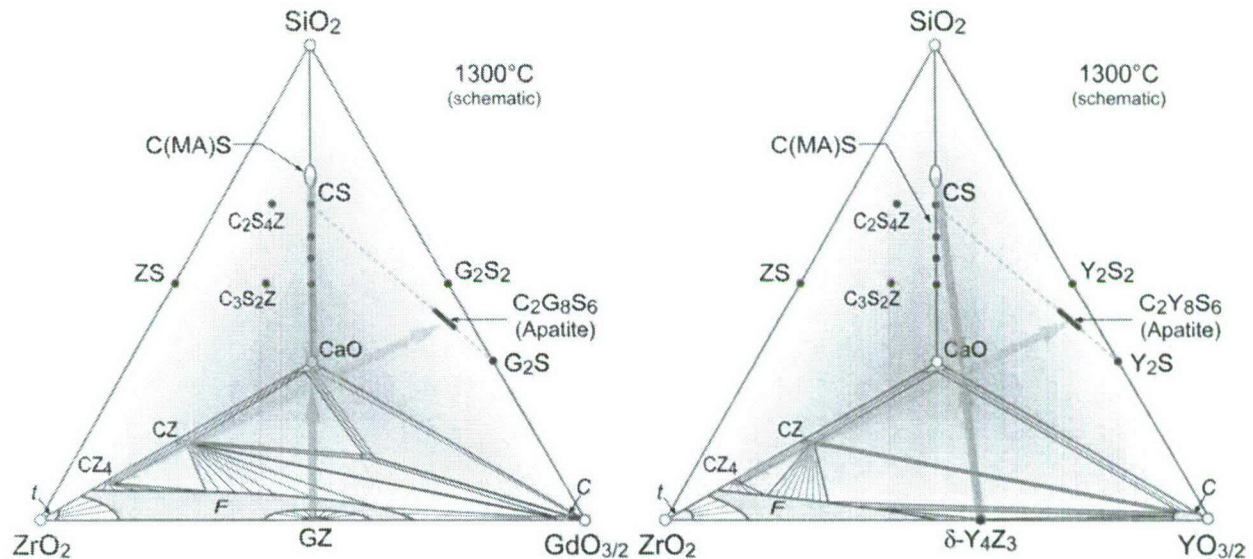


Fig. 4. Schematic comparison of the phases involved when CMAS reacts with the pyrochlore zirconate  $Gd_2Zr_2O_7$  (a) and the  $\delta$ -phase zirconate  $Y_4Zr_3O_{12}$  (b). The primary crystallization product is an oxyapatite of nominal composition  $Ca_2(Gd/Y)_8(SiO_4)_6O_2$ . In the ideal scenario the rest of the ingredients are combined in a (Zr,Ca) solution with the fluorite or the  $CaZr_4O_9$  structure. The MgO and  $AlO_{1.5}$  in CMAS are ignored as a first approximation because they combine independently to form a separate spinel phase and minor other silicates.

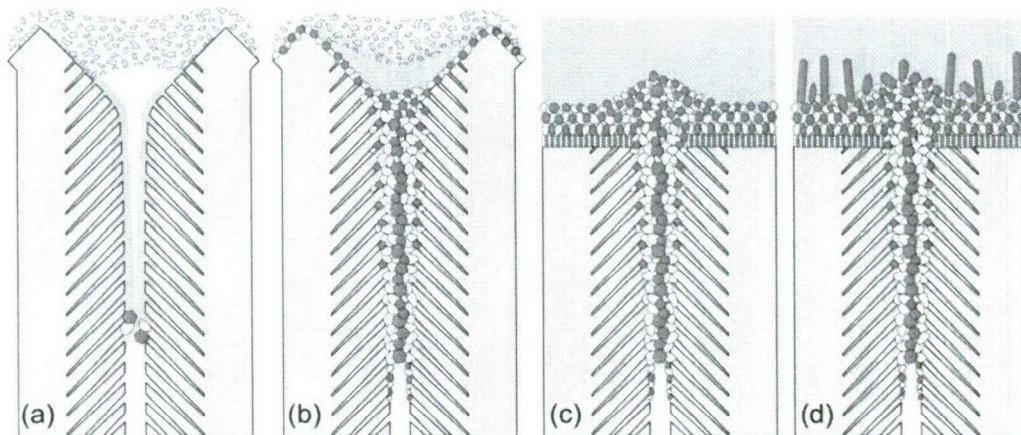


Fig. 5: Schematic of the steps in the mechanism of interaction between CMAS and GZ. The CMAS melts gradually, and the first liquid trickling down the intercolumnar gaps penetrates the feathers and starts dissolving GZ. As liquid proceeds down the gap its saturation level increases until the onset of crystallization occurs (a). The crystallites formed at the bottom soon block the penetration path and the continuing reaction fills the entire gap with crystalline products (b). Once the gaps are sealed the reaction at the tips proceeds much more gradually. At the interface with the GZ there is a dense layer of apatite and fluorite phases growing concurrently, fed by a thin network of intergranular amorphous films. Above this layer the amount of CMAS increases and the crystallites coarsen (c). The larger and elongated apatite crystals are probably formed during cooling, as illustrated in (d).

The mechanism by which penetration is inhibited involves the formation of a highly refractory apatite phase of nominal composition  $\text{Ca}_2(\text{Gd}/\text{Y})_8(\text{SiO}_4)_6\text{O}_2$  [13]. The phase relationships are illustrated for both materials in Fig. 4, neglecting as a first approximation the  $\text{MgO}$  and  $\text{AlO}_{1.5}$  components of CMAS, which appear primarily as spinel and a minor silicate phase. In their most efficient version, i.e. one that consumes the least amount of TBC, the nominal reactions can be expressed as follows (oxygen omitted for clarity):



The higher reactive element content of the Y zirconate reduces the amount needed to react with the same volume of CMAS to form the same volume of apatite, and consequently the amount of the second phase produced is slightly lower. In reality, the second phase formed is a fluorite solid solution that requires additional amount of zirconate. Conversely, the actual apatite phase contains some  $\text{Zr}^{4+}$  in solid solution that reduces the amount of dissolved zirconate.

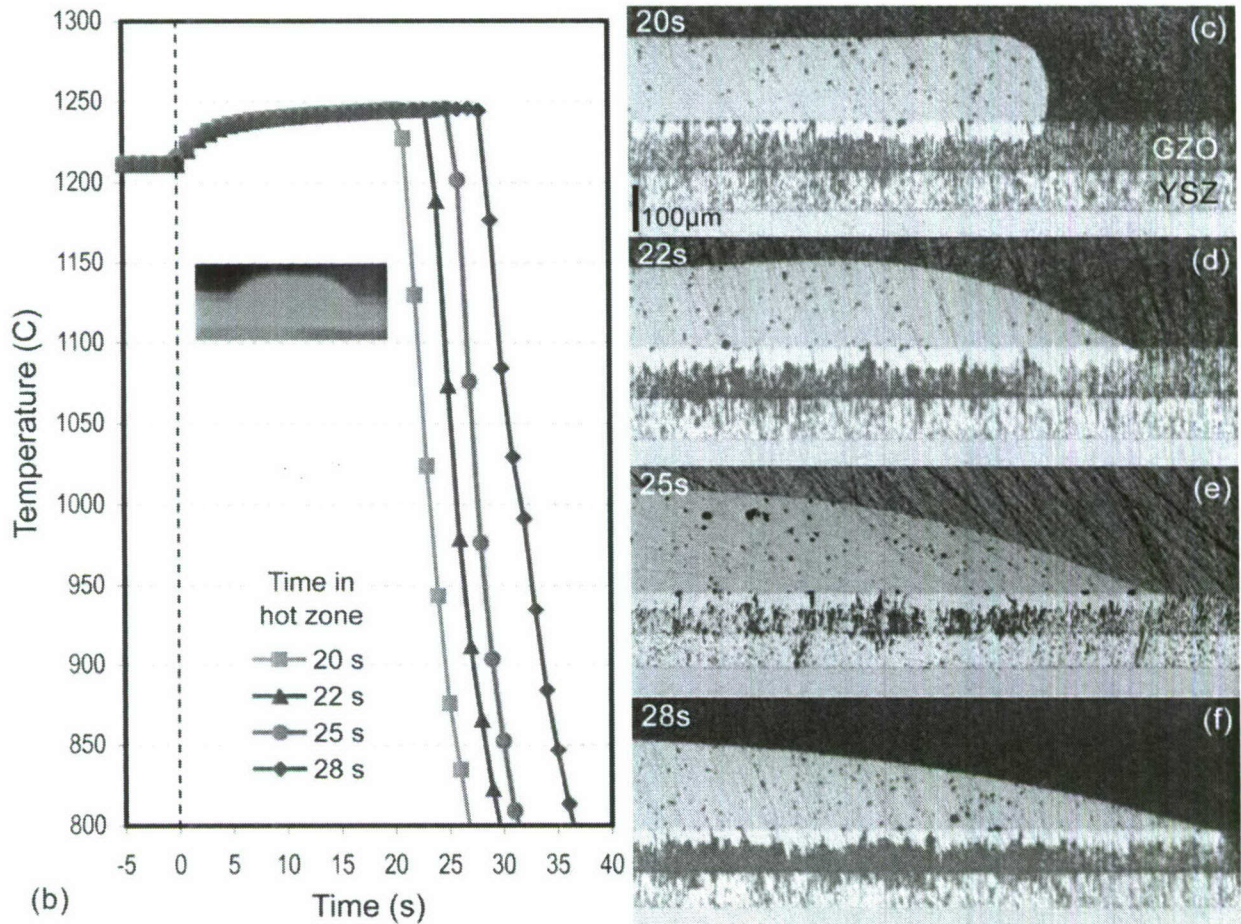


Figure 6: Initial stages of melting of a CMAS powder compact on a GZ/YSZ bilayer deposited by EB-PVD on polycrystalline alumina. The experimental set up is schematically depicted in Fig. 2. The sample is initially equilibrated at 1200°C, below the melting point of the model CMAS used. After equilibration the sample is rapidly moved into the hot zone, which is at ~1250°C, above the melting point of CMAS, held for a prescribed time and then removed to cool rapidly in the cold zone. Cross sections of the specimens resulting from the thermal histories in (b) are shown in (c-f). The bright region in the upper part of the GZ layer has been partially penetrated by CMAS. Note that penetration begins well before the initial pellet starts to collapse as a result of melting, but then does not increase significantly as the pellet melts.

The steps of the mechanism by which penetration is arrested are illustrated in Fig. 5 [13]. In essence, the sealing of the intercolumnar gaps occurs very early in the process, well before melting of CMAS was completed (or by extension when only a small amount of melt is available if deposits accumulate slowly on the surface). It was also recognized that the temperature would play a major role not only by influencing the viscosity and wetting characteristics of the melt, but also because of its effects on the rates of the dissolution of the oxide and the subsequent recrystallization of the reaction products.

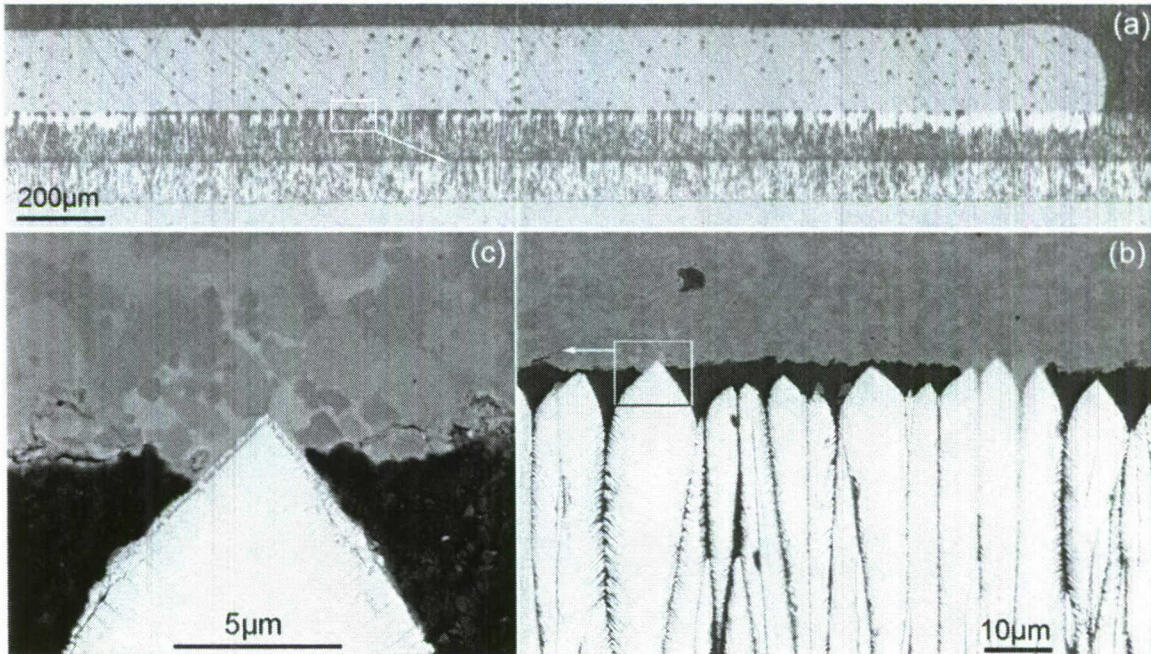


Figure 7: Details of the early stages of CMAS melting and rapid reaction when in contact with the GZ TBC. The images correspond to the 20 s sample in Fig. 6c. The close-up in (b) is taken in the region where there is no significant penetration, manifested by the absence of the brighter contrast directly under the CMAS pellet. Note in (b) that the CMAS pellet retains enough stiffness at this stage for regions between the higher elevations of the TBC to avoid sagging and touching the lower laying tips. There is, however, liquid corresponding to the lighter gray "matrix" within the CMAS crystalline phases (b,c). Where there is contact, as in (c), the incipient melt readily spreads downward along the tip surfaces and reacts to form a thin layer of product phases. The region on the three peaks on the right of (b) shows a slightly more advance stage wherein sufficient liquid has formed and trickled down to fill the valleys within these columns, penetrated down about 20-30µm and sealed the gaps (cf. Fig. 8).

Experiments using the set-up in Fig. 2 clearly demonstrated that the reaction between CMAS and the zirconates starts immediately and the products start precipitating within a few seconds of the initial contact. Figure 6 shows that liquid forms even before the pellet exhibits any macroscopic sign of deformation. A reaction layer is evident within 20s, Fig. 6(c), but does not increase significantly in thickness after the pellet collapses and begins to spread owing to the increasing amount of liquid (full melting was not achieved in any of the specimens in Fig. 6). In no case within these experiments did the liquid penetrate down to the underlying 7YSZ layer. The inference is that the melt penetration is fast, but the reaction that seals the paths to flow into the coating occurs within the same time scale, on the order of a few seconds. Indeed, the dissolution-precipitation reaction occurs essentially as soon as the melt contacts the zirconate, as illustrated in Fig. 7. Note that the penetration is not uniform along the macroscopic interface (Fig. 5a), perhaps due in part to some heterogeneity in composition within the pre-sintered sili-

cate pellet, but more likely because the surface of the CMAS pellet is not in contact with the coating at all points, as shown in Fig. 7b. (Arguably this would not occur in actual operation but the difference in behavior between points along the surface where the CMAS is or is not in contact with the tips is rather remarkable.) The scenario previously proposed wherein the first liquid to form is the one that activates the sealing mechanism is consistent with the observations in Fig. 7. Note that at contact points the liquid (otherwise held by capillarity within the network of still un-melted silicate particles in the CMAS) actively wets and flows downward on the surfaces of the GZ column tips (Fig. 7c), forming a reaction layer within a few seconds. One might speculate based on the difference in behavior between the single tip and the cluster of tips in contact with the CMAS pellet in Fig. 7b that the dissolution of Gd and Zr into the melt may have an effect in promoting melting, but verification of this hypothesis would require improved understanding of the effects of composition on the liquidus temperature of the CMAS.

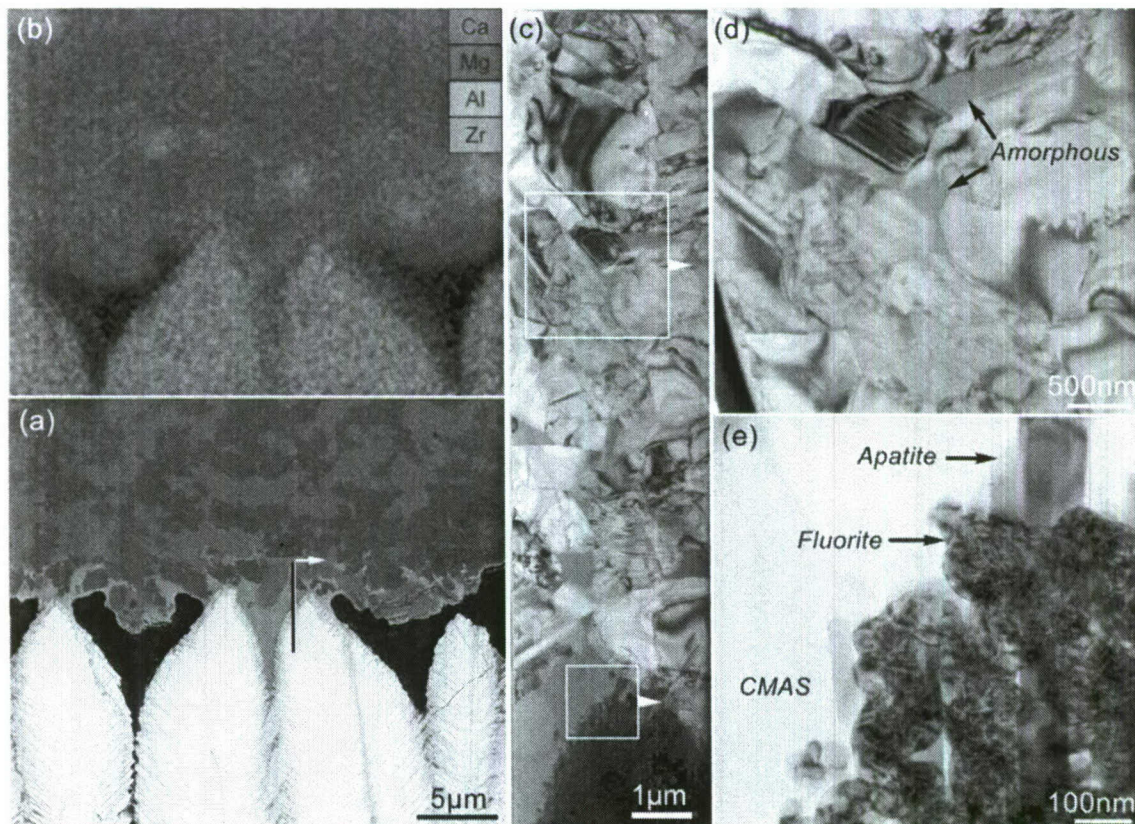


Figure 8: Analysis of the interaction between the incipient melt and the tips of a GZ TBC. The sample is the same as in Fig. 6c and 7(a). The BSEI in (a) shows a local liquid pocket that has filled the gap between the two column tips. It is also evident, however, that the melt has trickled down the side of the right tip and down an internal segmentation gap within the column, filling it with reaction products (slightly darker gray than column), a well as down to the gap within the smaller column, where some of the feather porosity shows signs of reaction. The elemental map in (b) shows the distribution of elements in the silicate deposit, suggesting at 2-3 crystalline phases (darker shades of grey in 8a and different elemental concentrations in 8b, in addition to the incipient melt which appears lighter gray). A FIB section in (c) away from the tip reveals the CMAS pellet to be largely crystalline, consisting of various silicate phases, with pockets of amorphous material (liquid at high temperature) in between (d). Closer examination of the tip region shows that the apatite and the Gd-lean fluorite crystals (e) have already started to form. Note the distinct difference in morphology between the faceted apatite crystals and the more globular fluorite formed on top of the tips.

Closer examination of these early reaction regions in the TEM, illustrated in Fig. 8, shows the complexity of the system and the presence of both fluorite and apatite crystals after a very brief exposure (20s). Note in Fig. 8a that the liquid has already filled the valley between two tips and produced a visible reaction layer that sealed the channel between these two columns. Conversely, the liquid trickling down into the neighboring valley has penetrated a much narrower gap within the column itself (owing to self-segmentation when columns widen owing to evolutionary selection [17]). The implication is that flow into a much narrower channel is faster than that into the normal intercolumnar gaps making the dissolution-reprecipitation sealing reaction somewhat less competitive.

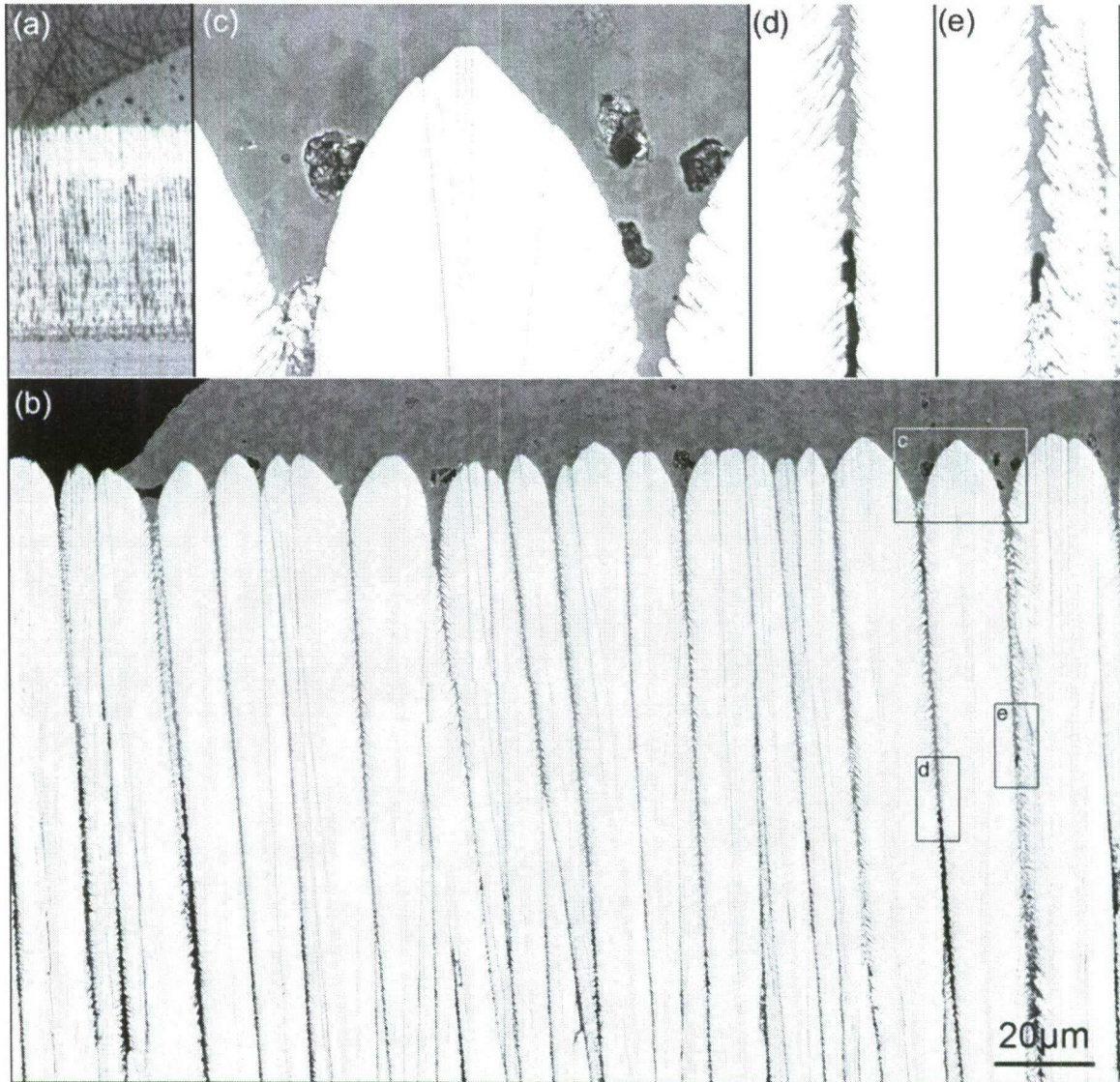


Fig. 9. Details of the early interaction between a crystalline CMAS pellet and a 7YSZ EBPVD TBC. The temperature is the same as in Fig. 6 but the exposure time (28 s) is slightly longer than in 6(c). By this point the CMAS pellet is sufficiently deformable to start spreading macroscopically (a) and to collapse into the valleys of the columnar surface (b). Note, however, that there is no evidence of obvious sign of attack nor second phase formation on the column tips (c). The CMAS is not completely molten, but the liquid has flown down the intercolumnar gaps to 50-60 μm below the tips (d,e).

The elemental map in Fig. 8b and the TEM analysis (Fig. 8c) suggests that at this early stage the CMAS pellet may contain as many as three distinct crystalline phases, with liquid in the interstices of the initially porous compact (Fig. 8d). Near the tip, where there is a relatively larger melt volume, TEM reveals that the TBC surface is already significantly attacked after only 20s and both fluorite and apatite have started forming on the reaction interface.

Similar exposure of columnar 7YSZ to CMAS reveals the essential difference between these two materials (Fig. 9). After 28s in the hot zone, the CMAS pellet has melted and started spreading on the surface. All tips under the original pellet are now in contact with the incipient melt, but there is no significant evidence of reaction (revealed by roughening of the surface and formation of new crystallites on it, e.g. Fig. 9c). The implication is that YSZ is much less reactive with CMAS, and by extension that it has less of an effect on the eventual crystallization, which in an isothermal experiment like this would not occur. Note that the melt has penetrated to somewhat greater depths in some channels than in the GZ experiments, but if the process were to continue nothing would impede the downward flow in 7YSZ, whereas the zirconate would be able to block the channels with reaction products and limit the depth of penetration.

Melting and spreading experiments undertaken during the renewal program also revealed minor differences in the behavior of the CMAS pellet and subsequent droplet on GZ and YZ. Coupled with the observations in Fig. 3, the experience to date suggests that YZ acts in the same manner as GZ but because it is somewhat less reactive (or perhaps the Gd-based apatite phase has a larger driving force for formation) the penetration into the YZ TBC should be somewhat higher than that into GZ.

### ***S/V Thrust***

The goal of this thrust was to demonstrate that the sensitivity of YSZ to de-stabilization by sulfate-vanadate melts could be favorably modified by adding a second oxide that reduces the activity of Y in solid solution and thus the rate of the reaction with the molten deposit. The materials of interest are based on the  $ZrO_2$ - $YO_{1.5}$ - $TaO_{2.5}$  system (Fig. 10), wherein the affinity of Ta for Y, manifested by the formation of  $YTaO_4$ , offers the desired reduction in activity within the  $ZrO_2$  solid solution. The strategy was validated by hot corrosion experiments in air, and subsequently by experiments in more aggressive atmospheres containing  $SO_3$  in concentrations substantially above those expected in gas turbine operation.

The appeal of this system expanded beyond its potentially desirable corrosion behavior owing to two additional attributes. First, the system is rather unique in offering a tetragonal structure that is phase-stable at temperatures as high as 1500°C, substantially above the capabilities of the metastable non-transformable 7YSZ [18-20]. Moreover,  $ZrO_2$ - $YO_{1.5}$ - $TaO_{2.5}$  compositions within the phase stable tetragonal domain had been reported to show toughness values comparable to those of 7YSZ within that range [21]. Effort was thus placed in investigating the toughness properties of selected compositions in this system.

All materials tested were based on sintered compacts of precursor-derived powders. Phase stability studies focused on compositions within the t + c field (a, e, g, j) or at its boundaries (b, f, h, l). Corrosion experiments compared Y (a-c) with Y+Ta (g, l, j, l) compositions in air and  $SO_3$  atmospheres, with emphasis on 7YSZ (a) v.  $ZrO_2$ -16.6 $YO_{1.5}$ +16.6 $TaO_{2.5}$  (l). The more extensive work on toughness focused on compositions (a-c, g-m).

This program had been initiated in a previous three-year grant, so only results during the present grant are highlighted below. More extensive details are summarized in a doctoral dissertation resulting from this activity [22] and one paper already published [23]. Two additional papers are in preparation [24, 25].

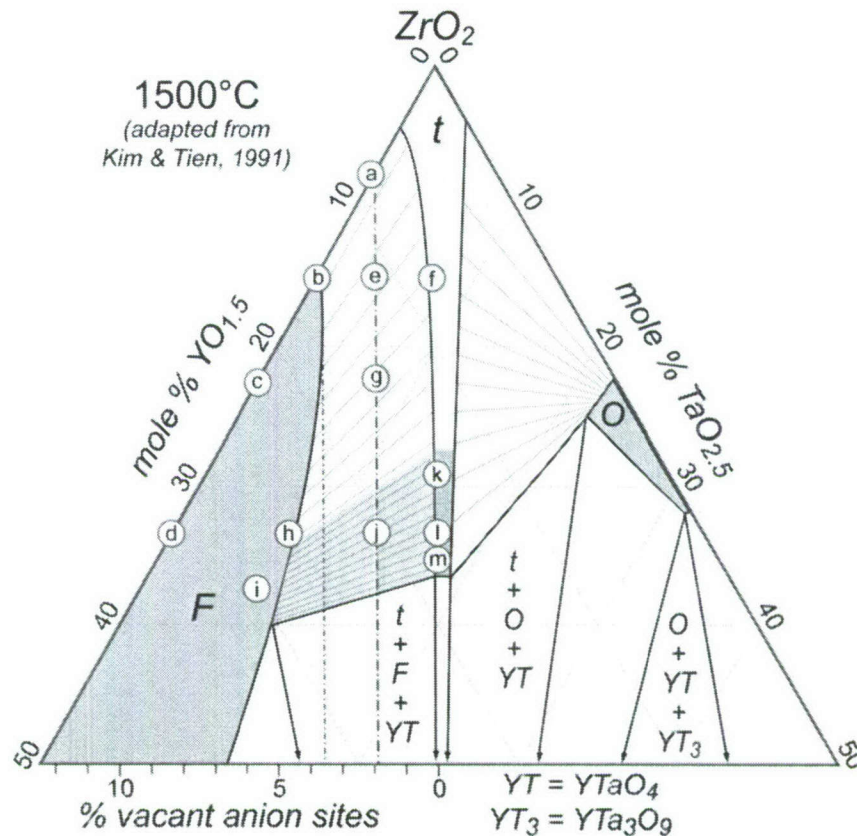


Fig. 10. Isothermal section of the  $ZrO_2$ - $YO_{1.5}$ - $TaO_{2.5}$  phase diagram at  $1500^\circ C$  showing the regions of interest and compositions investigated to date (labeled circles). The “stable”  $t + F$  field (green) offers a “safe” operating window because partitioning yields an equilibrium tetragonal phase that is “non-transformable” to monoclinic.

### Findings

*Comparative corrosion experiments in 7YSZ and Y+Ta Co-doped zirconia.* The experiments used rather heavy ( $25\text{-}35\text{ mg/cm}^2$ ) loadings of  $Na_2SO_4\text{-}30\%NaVO_3$  and exposures to  $900^\circ C$  in 25h cycles, with re-salting every 50 h [22]. The more critical experiments are those with an atmosphere containing about 270 ppm of  $SO_3$ , created by passing an  $O_2\text{-}1\%SO_2$  gas through a Pt-based catalyst at rates suitable to reach the equilibrium  $SO_3/SO_2$  ratio corresponding to the exposure temperature.

Results for 7SZ exposed to the S/V melt in air showed formation of acicular m- $ZrO_2$  crystals after relatively short times, e.g. Fig. 11c, followed by formation of larger plate-like  $YVO_4$  at longer times, e.g. Fig. 11e. The large monoclinic crystals are essentially pure  $ZrO_2$  and their size and faceted features are consistent with evolution from the melt and not by a “leaching” process from solid YSZ. Under the crust of reaction products there is a porous layer of Y-depleted YSZ, where the Y content increases with increasing distance from the surface as shown in Fig. 12. The YSZ crystallite size is consistent with that of the parent 7YSZ, and the porosity was presumably filled with S/V melt which was washed away by post-exposure immersion in water. Each of the crystallites in this region appears to have a 7YSZ core with a shell of lower Y content whose thickness increases toward the surface. The structure is consistent with melt penetration into the pore space, attack of the grain boundaries and gradual dissolution of the 7YSZ, which subsequently re-precipitates with a lower Y content.

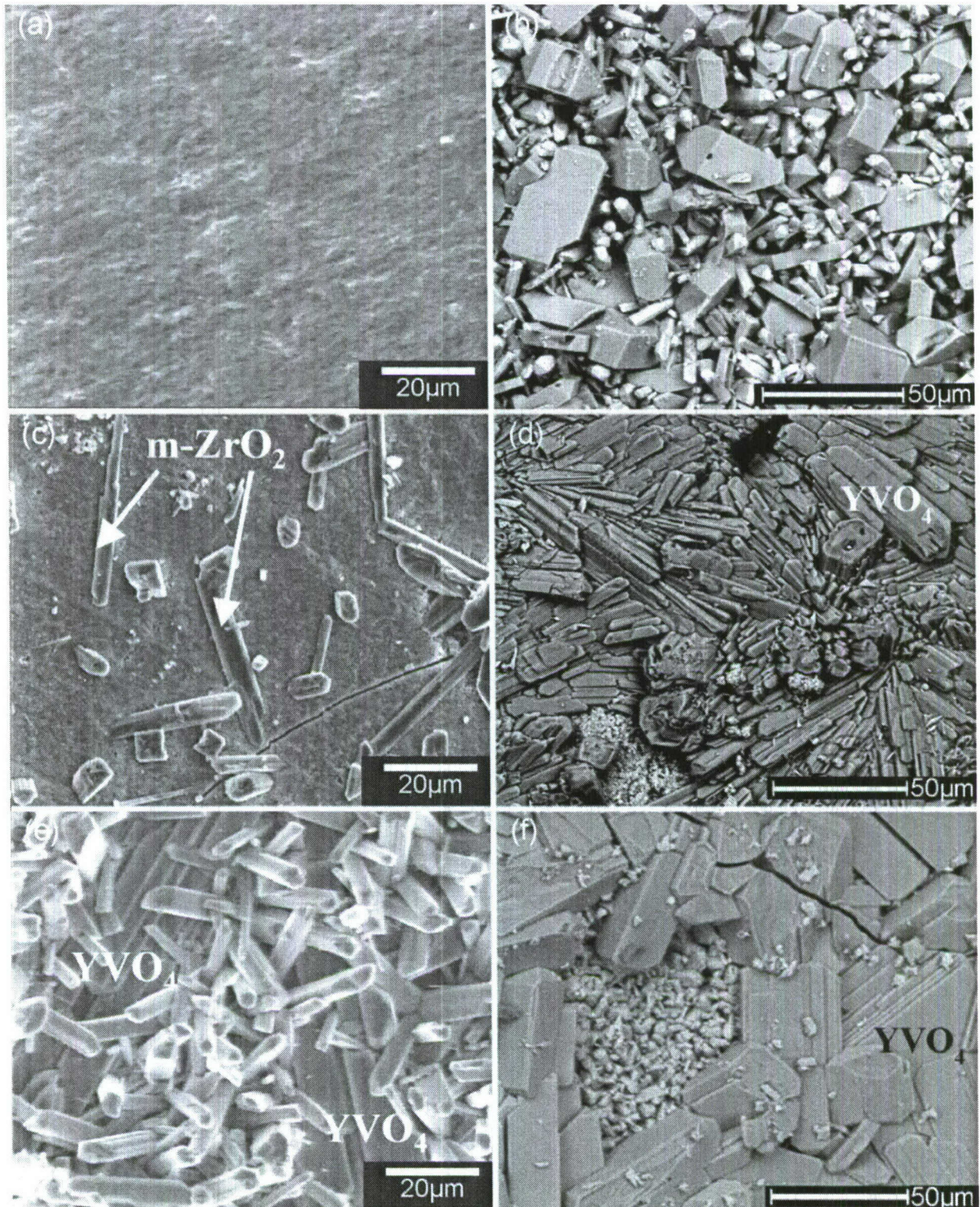


Fig. 11: Views of the surface of 7YSZ samples in the pristine condition (a) and after exposure to  $\text{Na}_2\text{SO}_4$ -30mole% $\text{NaVO}_3$  melts at  $900^\circ\text{C}$  in air for (c) 50h and (e) 100h, and in  $\text{SO}_3/\text{SO}_2+\text{O}_2$  for (b) 25h, (d) 50h and (f) 100h. Note the predominance of monoclinic  $\text{ZrO}_2$  on the surfaces exposed in air, v.  $\text{YVO}_4$  for those exposed to the more corrosive  $\text{SO}_3/\text{SO}_2+\text{O}_2$  atmosphere, where the layer of corrosion products is also thicker. Cross sections show extensive monoclinic formation under the  $\text{YVO}_4$  layer in (b, d, f).

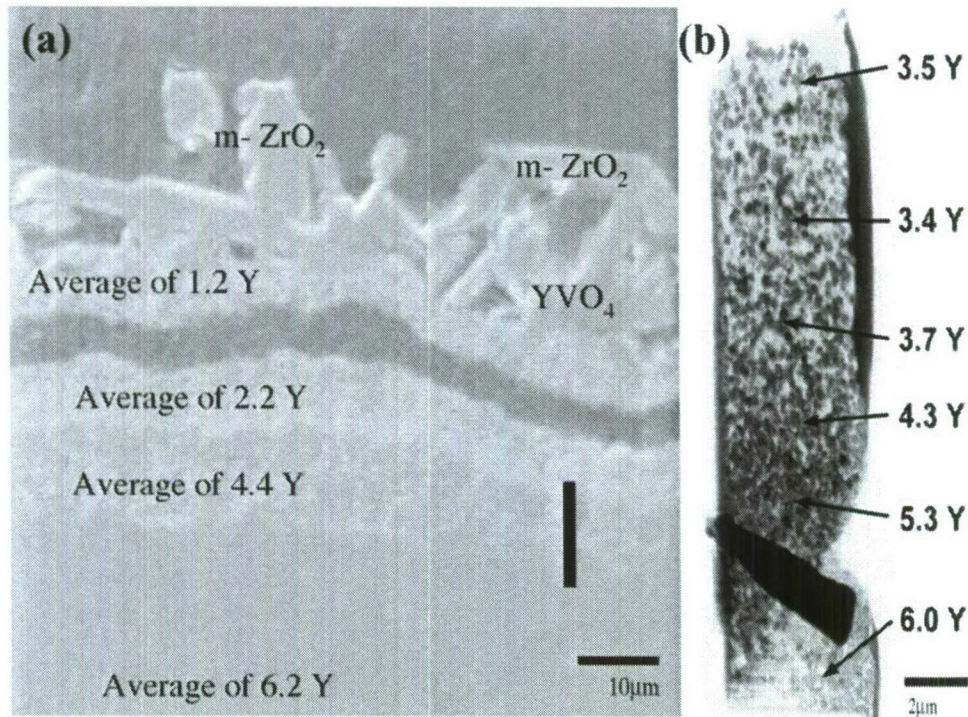


Fig. 12: Cross sections of the 7YSZ sample after 100h exposure to a  $\text{Na}_2\text{SO}_4$ -30mole% $\text{NaVO}_3$  melt at  $900^\circ\text{C}$  in air where the (a) SEM the degraded regions under the reaction product "crust". The Y depleted layer consists of partially dissolved crystallites that have a reprecipitated shell with a progressively lower Y content closer to the surface, as shown by the TEM section in (b). The depleted layer is considerably thicker ( $\sim 500\mu\text{m}$ ) after exposure in  $\text{SO}_3/\text{SO}_2+\text{O}_2$  for 75h.

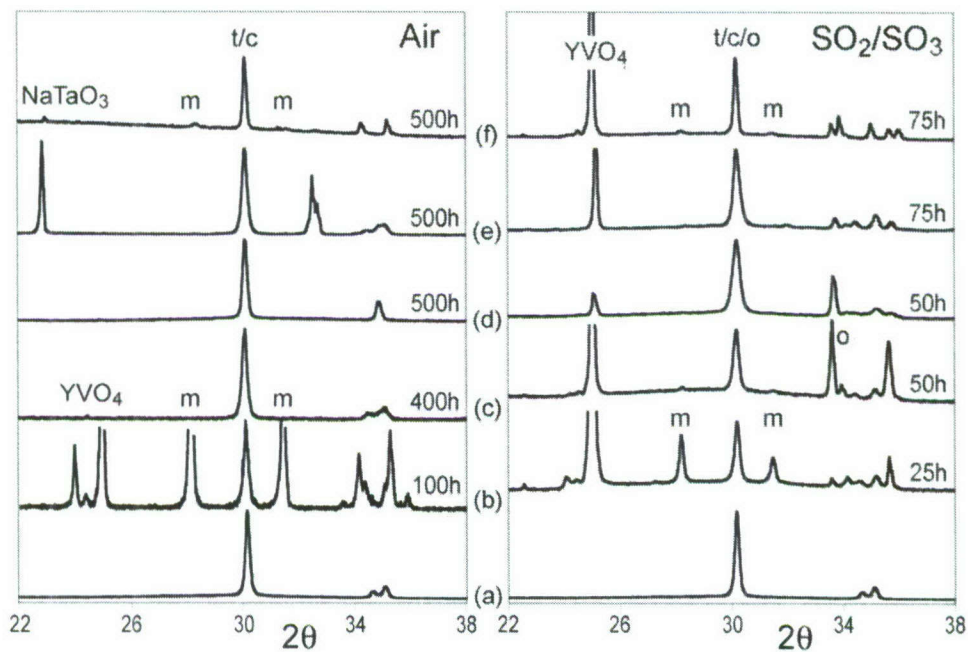


Fig. 13: XRD spectra of the surfaces of compacts after  $900^\circ\text{C}$  exposures to S/V melts with a coverage of  $25\text{-}35\text{mg}/\text{cm}^2$  in air (left) and  $\text{SO}_3/\text{SO}_2+\text{O}_2$  (right) for the times indicated. The baseline 7YSZ material is shown in pristine condition (a) and after corrosion (b). Y+Ta co-doped compositions are (c) 15Y8Ta, (d) 30Y8Ta, (e) 20Y13Ta, and (f) 16Y16Ta.

Equivalent exposures in  $\text{SO}_3/\text{SO}_2$  reveal formation of  $\text{YVO}_4$  at an earlier stage, consistent with the higher acidity of the melt, and predominance over monoclinic  $\text{ZrO}_2$  on the surface crust, as shown in Figs. 11(b,d,f) and 13(b). Concomitantly, the thickness of the Y depleted layer increases to  $\sim 500\mu\text{m}$  after 75h, compared with only  $\sim 20\mu\text{m}$  in air at 100h (Fig. 12).

Results for similar exposures of the co-doped Y+Ta compositions are summarized in Figs. 13 and 14. In general, the samples exposed to the S/V melt in air showed little corrosion even after 400-500h, the only significant evidence of a reaction product being crystals of  $\text{NaTaO}_3$  on the surface of the compositions richer in Ta, Fig. 13(e,f, left) and Fig. 14(a). In contrast, the co-doped compositions showed formation of  $\text{YVO}_4$  instead of  $\text{NaTaO}_3$ , accompanied by orthorhombic zirconia (cf. Fig. 12). The former is consistent with the much more acidic nature of the S/V melt under the higher  $p\text{SO}_3$ , while the latter is the result of preferential Y depletion that shifts the average composition of the dissolved oxide across the tetragonal field in Fig. 12. It is notable, however, that the exposed surface still has a composition and grain size comparable with the original compact, as shown in Fig. 14(d). More importantly, the Y-depletion from the layer under the crust of reaction products and the thickness of said layer is considerably reduced, from  $\sim 500\mu\text{m}$  in 7YSZ to  $\sim 25\mu\text{m}$  in the 16Y+16Ta material after 75h exposure.

*Toughness of phase stable, non-transformable co-doped  $t'$ .* The toughness values measured on 7YSZ and three Y+Ta co-doped compositions (k, l, m) are listed below, together with values for the tetragonality calculated from the {400} peaks in the XRD pattern [23].

sample	$\text{YO}_{1.5}$	$\text{TaO}_{2.5}$	$\Gamma$ ( $\text{J/m}^2$ )	$\sigma$ ( $\text{J/m}^2$ )	c/a
7YSZ	7.6	-	41.8	8.4	1.013
14YTaSZ	14.5	14.5	52.5	13.3	1.0235
16YTaSZ	16.6	16.6	41.4	12.4	1.024
17YTaSZ	17.6	17.6	39.3	10.4	1.025

Confidence in the results is given by the agreement between the measurement for 7YSZ and other reports in the literature [26, 27]. It is first noted that all the co-doped compositions tested have toughness values comparable or higher than 7YSZ, in spite of a significantly higher tetragonality that would suggest a larger improvement based on the hypothesis that ferroelastic switching is the underlying mechanism [28]. Moreover, the toughness decreases with the small but systematic increase in tetragonality for the Y+Ta compositions, a trend also noted in an earlier study [21] but not yet understood.

One possibly significant factor for the rather modest improvement in toughness between the 7YSZ and the co-doped compositions, in spite of the significant increase in tetragonality, is the substantially smaller grain size of the former. Because these compositions do not initially contain twin tetragonal domains, as characteristic of the other  $t'$  structures in which ferroelastic toughening has been studied, one might anticipate that twin nucleation could be a critical step in enabling the mechanism, and the twinning process could be influenced by differences in the grain size as is the case in transformation toughening [29]. Indeed, twin nucleation has been observed around indentation cracks in 7YSZ samples originally twin-free and subjected to toughness measurements by the same technique used in this study [30]. Alternatively, it is possible that the coercive stress for domain boundary motion increases with tetragonality, and thus the requisite stresses may be achieved in a smaller fraction of the grains around the crack. Research on these issues is continuing under a separate program.

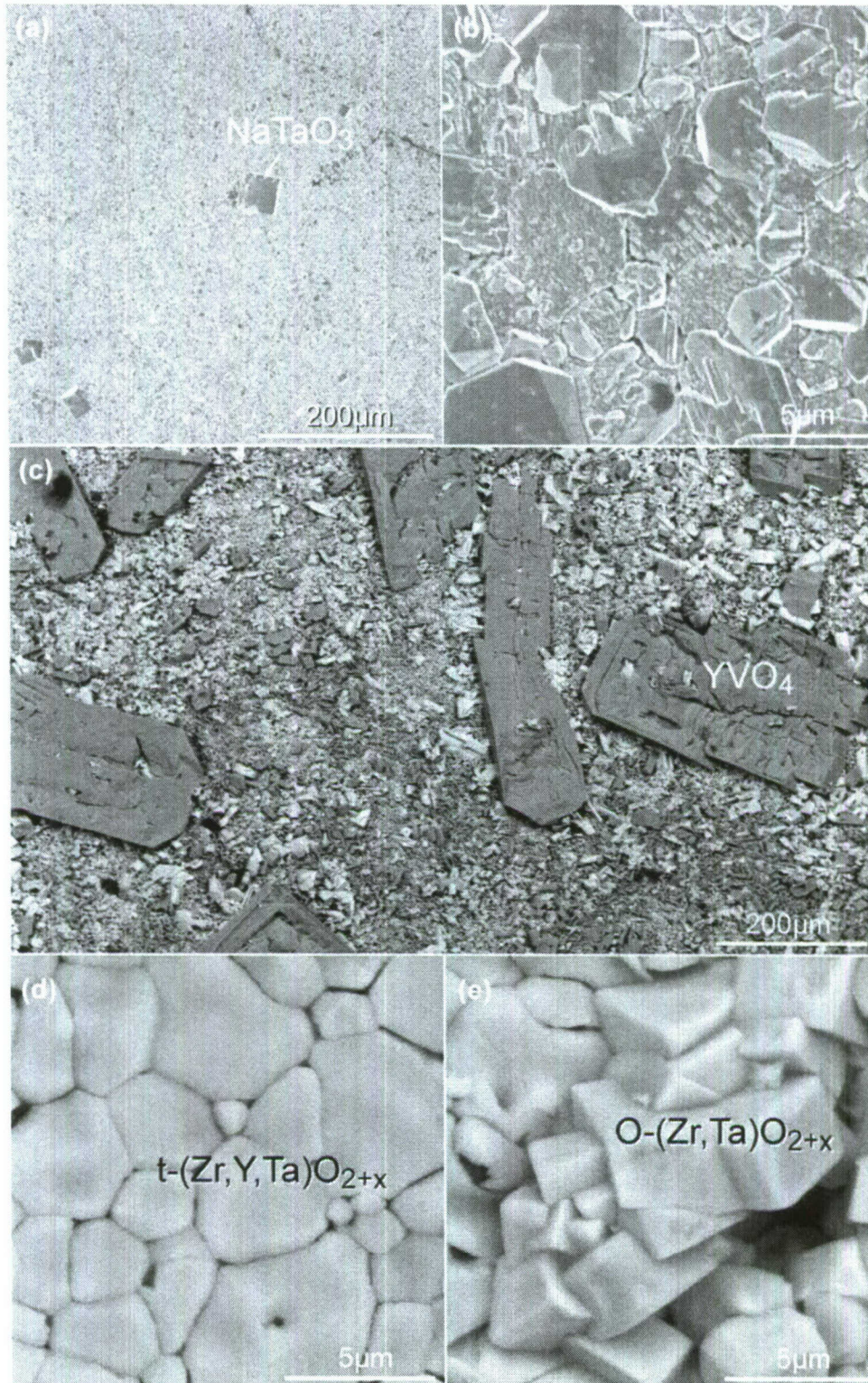


Fig. 14: SEM views of the surface of 16Y+16Ta samples after 75h exposure to  $\text{Na}_2\text{SO}_4$ -30mole% $\text{NaVO}_3$  melts at  $900^\circ\text{C}$  in air (a,b) and in  $\text{SO}_3/\text{SO}_2+\text{O}_2$  (c-e). The surface in (a) contains a few relatively large faceted crystallites of  $\text{NaTaO}_3$ , with no significant amount of depletion or other reaction products (b). The more aggressive environment leads to the formation of  $\text{YVO}_4$  (c), with a slightly depleted tetragonal underlayer (d),  $\sim 25\mu\text{m}$  thick, and clusters of highly faceted orthorhombic  $(\text{Zr,Ta})\text{O}_{2+x}$  (e).

### **Broader Impacts**

Both thrusts have contributed not only to the understanding of the mechanisms by which TBCs are degraded by S/V and CMAS melts, but also to the identification of viable mitigation solutions. These strategies have been transferred to industry, and are in the process of implementation. There is also strong interest in the increased phase stability and comparable toughness of the single-phase tetragonal Y+Ta co-doped compositions compared with 7YSZ. Two different companies are exploring the development of these compositions using both plasma spray and EB-PVD, although there has been no specific goal of using them to mitigate S/V attack since that problem is currently managed by controlling fuel purity.

The CMAS mitigation attributes of the zirconates have generated substantial interest because they represent a fundamental barrier to progress in gas turbine technology. The PI continues to work with industry in exploring the viability of these solutions, notably with regard to the durability of the "sealed" layer in thermal cycling conditions and moisture environments. These are part of the renewal program. The PI has also communicated the issues and solutions under investigation to US Navy personnel at the Patuxent River Navair Station.

Regarding contributions to human resource development, one student (Felicia M. Pitek, US citizen) received her Ph.D. under this program [22] and is currently working for Bechtel Plant Machinery (Pittsburgh) on materials issues relevant to the US Navy. A new student (Elisa M. Vogel, US citizen) is continuing the work under the present program. Dr. Pitek was quite active in mentoring undergraduates during her Ph.D., including several students from underrepresented groups. One US undergraduate in Mechanical Engineering is currently involved in the program.

### **References**

1. M.P. Borom, C.A. Johnson, and L.A. Peluso, "Role of environmental deposits and operating surface temperature in spallation of air plasma sprayed thermal barrier coatings," *Surface and Coatings Technology*, 86-87 116-126 (1996).
2. C. Mercer, S. Faulhaber, A.G. Evans, and R. Darolia, "A delamination mechanism for thermal barrier coatings subject to calcium-magnesium-alumino-silicate (CMAS) infiltration," *Acta Materialia*, 53 [4] 1029-1039 (2005).
3. A.G. Evans and J.W. Hutchinson, "The Mechanics of Coating Delamination in Thermal Gradients," *Surface and Coatings Technology*, 201 7905-7916 (2007).
4. S. Krämer, S. Faulhaber, M. Chambers, D.R. Clarke, C.G. Levi, J.W. Hutchinson, and A.G. Evans, "Mechanisms of cracking and delamination within thermal barrier systems in aero-engines subject to calcium-magnesium-alumino-silicate (CMAS) penetration," *Materials Science and Engineering A*, 490 26-35 (2008).
5. S. Krämer, J.Y. Yang, C.A. Johnson, and C.G. Levi, "Thermochemical interactions of thermal barrier coatings with molten CaO-MgO-Al<sub>2</sub>O<sub>3</sub>-SiO<sub>2</sub> (CMAS) deposits," *Journal of the American Ceramic Society*, 89 [10] 3167-3175 (2006).
6. R.M. Leckie, S. Krämer, M. Ruhle, and C.G. Levi, "Thermochemical compatibility between Alumina and ZrO<sub>2</sub>-GdO<sub>3/2</sub> thermal barrier coatings," *Acta Materialia*, 53 [11] 3281-3292 (2005).
7. M.J. Maloney, "Thermal barrier coating systems and materials," U.S. Patent 6,117,560, 2000.
8. M.J. Maloney, "Thermal barrier coating systems and materials," U.S. Patent 6,177,200, 2001.
9. R. Vassen, X. Cao, F. Tietz, D. Basu, and D. Stöver, "Zirconates as new materials for thermal barrier coatings," *Journal of the American Ceramic Society*, 83 [8] 2023-2028 (2000).
10. R. Vaßen, F. Traeger, and D. Stöver, "New Thermal Barrier Coatings Based on Pyrochlore/YSZ Double-Layer Systems," *International Journal of Applied Ceramic Technology*, 1 [4] 351-361 (2004).

11. J. Wu, X. Wei, N.P. Padture, P.G. Klemens, M. Gell, E. Garcia, P. Miranzo, and M.I. Osendi, "Low-thermal-conductivity rare-earth zirconates for potential thermal barrier coating applications," *Journal of the American Ceramic Society*, 85 [12] 3031-35 (2002).
12. R. Subramanian, "Highly defective oxides as sinter resistant thermal barrier coating," U.S. Patent Application US 203/0108768, 2003.
13. S. Krämer, J.Y. Yang, and C.G. Levi, "Infiltration-inhibiting reaction of Gadolinium Zirconate Thermal Barrier Coatings with CMAS melts," *Journal of the American Ceramic Society*, 91 [2] 576-583 (2008).
14. M.J. Maloney, Private communication to A.G. Evans. 2004.
15. M.J. Maloney, Development and Experience with Low Conductivity Thermal Barrier Coatings, in Turbine Forum. 2006, Forum of Technology, Germany: Nice-Port St. Laurent, France.
16. R. Darolia, B.A. Nagaraj, D.G. Konitzer, M.D. Gorman, and F. Ming, "Layered thermal barrier coatings containing lanthanide series oxides for improved resistance to CMAS degradation," U.S. Patent Application 200770160859-A1, 2007.
17. S.G. Terry, "Evolution of microstructure during the growth of thermal barrier coatings by electron-beam physical vapor deposition," Doctoral Dissertation in Materials, University of California, Santa Barbara, CA, 2001.
18. C.G. Levi, "Emerging Materials and Processes for Thermal Barrier Systems," *Current Opinion in Solid State and Materials Science*, 8 [1] 77-91 (2004).
19. V. Lughì and D.R. Clarke, "High temperature aging of YSZ coatings and subsequent transformation at low temperature," *Surface and Coatings Technology*, 200 [5-6] 1287-1291 (2005).
20. J.M. Cairney, N.R. Rebollo, M. Ruhle, and C.G. Levi, "Phase stability of thermal barrier oxides: a comparative study of Y and Yb additions," *International Journal of Materials Research*, 98 [12] 1177-1187 (2007).
21. D.-J. Kim and T.-Y. Tien, "Phase stability and physical properties of cubic and tetragonal ZrO<sub>2</sub> in the system ZrO<sub>2</sub>-Y<sub>2</sub>O<sub>3</sub>-Ta<sub>2</sub>O<sub>5</sub>," *Journal of the American Ceramic Society*, 74 [12] 3061-65 (1991).
22. F.M. Pitek, "A study of the Zirconia-Yttria-Tantala system as a potential thermal barrier oxide," Doctoral Dissertation in Materials, University of California, Santa Barbara, 2006.
23. F.M. Pitek and C.G. Levi, "Opportunities for TBCs in the ZrO<sub>2</sub>-YO<sub>1.5</sub>-TaO<sub>2.5</sub> system," *Surface and Coatings Technology*, 201 6044-6050 (2007).
24. F.M. Pitek and C.G. Levi, "Phase stability of Y + Ta co-doped zirconia compositions," *Materials Science and Engineering* (to be submitted), (2008).
25. F.M. Pitek, G. Benson, and C.G. Levi, "Corrosion of thermal barrier coatings by sulfate/vanadate melts and mitigation approach," *Corrosion Science* (in preparation), (2008).
26. M. Watanabe, C. Mercer, C.G. Levi, and A.G. Evans, "A probe for the high temperature deformation of oxides used for thermal barrier systems," *Acta Materialia*, 52 [6] 1479-87 (2004).
27. T.A. Schaedler, R.M. Leckie, S. Krämer, A.G. Evans, and C.G. Levi, "Toughening of Non-transformable t'-YSZ by Addition of Titania," *Journal of the American Ceramic Society*, 90 [12] 3896-3901 (2007).
28. A.V. Virkar, "Role of ferroelasticity in toughening of zirconia ceramics," *Key Engineering Materials*, 153-154 183-210 (1998).
29. N. Claussen and M. Rühle, "Design of transformation-toughened ceramics", p. 137-63 in *Science and Technology of Zirconia*. Edited by A.H. Heuer and L.W. Hobbs. The American Ceramic Society, Inc.: Columbus, OH, 1981.
30. C. Mercer, J.R. Williams, D.R. Clarke, and A.G. Evans, "On a ferroelastic mechanism governing the toughness of metastable tetragonal-prime (t') yttria stabilized zirconia," *Proceedings of the Royal Society A-Mathematical Physical and Engineering Sciences*, 463 1393-1408 (2007).